Unraveling the origin of the complex structure of the thorium $L\gamma$ x-ray lines in high-resolution spectra induced by heavy projectiles

Katarzyna Słabkowska,* Joanna Starosta, Ewa Węder, Łukasz Syrocki, and Marek Polasik
Faculty of Chemistry, Nicolaus Copernicus University in Toruń, PL-87-100 Toruń, Poland

(Received 22 September 2016; published 5 July 2017)

The origin of the complex structure of $L\gamma_1$ (L_2N_4), $L\gamma_2$ (L_1N_2), $L\gamma_3$ (L_1N_3), and $L\gamma_6$ (L_2O_4) x-ray lines of thorium in high-resolution spectra induced by oxygen projectiles has so far resisted reliable quantitative interpretation. Therefore, the detailed structure predictions for satellite (additional holes in M,N,O, and/or P shells) and hypersatellite (additional hole in L shell) $L\gamma$ x-ray lines of thorium being the results of extensive multiconfiguration Dirac-Fock calculations have been performed. Our predictions reproduce with the excellent precision the positions and shapes of characteristic parts of above high-resolution $L\gamma$ x-ray spectrum of thorium what indicates that our study has been carried out with very high accuracy. The results of this study are the precursor for proper quantitative interpretation of the complex origin of $L\gamma_1,L\gamma_2,L\gamma_3$, and $L\gamma_6$ lines in high-resolution x-ray spectra of thorium induced by different light and heavy projectiles.

DOI: 10.1103/PhysRevA.96.012506

I. INTRODUCTION

X ray from atoms with single vacancies excited by energetic electrons emit the well-known diagram lines that are known as characteristic x rays, but the x rays emitted from atoms multiply ionized by heavy ions exhibit in addition a so-called satellite and hypersatellite structure. These x-ray line structures correspond to different multivacancy configurations that exist during x-ray emission and as a result, the K [1–8], L [9–24], and M [25–31] x-ray lines, for many heavy (and also mid-Z) elements especially in heavy ion collisions, are complex. Theoretical studies [5–8,23,24,29,31–40] that include the effect of ionization in the various shells on the positions and shapes of the particular x-ray lines are therefore absolutely essential for reliable and detailed interpretation of the measured x-ray spectra, among others concerning x-ray spectra for thorium [10,12,20–22,26–29,38]. An extremely large amount of theoretical and experimental results on the systematic research concerning complex x-ray line structures of various heavy systems published in the last few years proves the current relevance of this subject [[10,12,14–17,20,25–28],[32–36,41–46]].

The fundamental importance of such theoretical research is demonstrated by many successes in the analysis of observed K,L, and M x-ray lines [9,38–40]. For example, extensive multiconfiguration Dirac-Fock (MCDF) calculations with the inclusion of transverse (Breit) interaction and quantum electrodynamics (QED) corrections have been carried out on thorium [29] and gold [31], elucidating the structure of the satellite and hypersatellite $M\alpha_{1,2}$ ($M_5N_{6,7}$) and $M\beta_1$ (M_4N_6) lines. Likewise, the experimental $M\alpha_{1,2}$ satellite lines in the x-ray spectra of thorium bombarded by 376-MeV oxygen ions could be interpreted with MCDF computations that included the various satellite and hypersatellite $M\alpha_{1,2}$ and $M\beta_1$ lines [38]. For uranium the corresponding M x-ray lines have been analyzed theoretically as well [41]. In addition to the quantitative interpretation of the complex structure of the $M\alpha_{1,2}$ and $M\beta_1$ lines in high-resolution x-ray spectra of uranium induced by different light and heavy projectiles, the parameters of uranium M x-ray lines obtained this way can be helpful in the use of UO_2 as a reference material in x-ray measurements [47].

Intermediate-Z elements have been studied as well. One example is palladium excited by 278.6-MeV O^{6+} ions. Multiple ionization of the L and M shells gives the $L\alpha_{1,2}$ ($L_3M_{4,5}$) and $L\beta_1$ (L_2M_4) x-ray satellite structures that were measured with high energy resolution. Interpretation by relativistic MCDF calculations led to an estimate for the average number of L- and M-shell spectator vacancies during x-ray emission, and, after correction for the atomic vacancy rearrangement, to the ionization probabilities corresponding to the collision time [42]. In particular, Czarnota *et al.* [43] analyzed in detail one-photon decay of L^{-2} double-vacancy states, which produces the L^{-1} hypersatellite x-ray lines. Zirconium and molybdenum ionized by the same oxygen beam were analyzed in detail by same group [44]. All these high-resolution spectra are characterized by numerous and partly overlapping various satellite and L^{-1} hypersatellite x-ray lines that are best disentangled with results from detailed MCDF calculations [44].

As have been demonstrated in the series of papers published by Indelicato *et al.* [48–51], the Auger processes can have noticeable influence on some x-ray transitions in the case of autoionizing states. In our study presented here all initial states are also autoionizing ones. Therefore, the Auger processes can have some effect on the $L\gamma$ x-ray line positions also in the case of such high-Z elements like thorium. However, in the framework of our approach we haven't included the effect of Auger processes on the $L\gamma$ x-ray line positions. Nevertheless, in our theoretical predictions we have taken into account the influence of Auger transitions on the values of all level widths which are in many cases very important. Therefore, we have included Auger processes in the natural linewidths for the $L\gamma_1,L\gamma_2,L\gamma_3$, and $L\gamma_6$ diagram lines (basing on data from Campbell and Papp [52]), and also for all satellite and hypersatellite lines (see Table I), including the ionization effect of N,M, and L shells on the natural linewidths (also with data from Campbell and Papp [52]).

*katarzyna.slabkowska@umk.pl

TABLE I. The $L\gamma_1, L\gamma_2, L\gamma_3$, and $L\gamma_6$ linewidths for all diagram, satellite, and hypersatellite transitions for Th in eV.

Transition type	Additional hole	Linewidth (eV)			
		$L\gamma_1$	$L\gamma_2$	$L\gamma_3$	$L\gamma_6$
Diagram	–	12.80	23.05	21.80	8.70
	M_1	43.80	54.05	52.80	39.70
	M_2	39.20	49.45	48.20	35.10
	M_3	28.80	39.05	37.80	24.70
	$M_{4,5}$	19.36	29.61	28.36	15.26
	N_1	35.80	46.05	44.80	31.70
Satellite	N_2	30.30	40.55	39.30	26.20
	N_3	27.80	38.05	36.80	23.70
	N_4	21.40	31.65	30.40	17.30
	N_5	21.00	31.25	30.00	16.90
	N_6	13.10	23.35	22.10	9.00
	N_7	13.16	23.41	22.16	9.06
	O_4	13.20	23.45	22.20	9.10
	L_1	41.40	51.65	50.40	37.30
Hypersatellite	L_2	29.80	40.05	38.80	25.70
	L_3	28.28	38.53	37.28	24.18

This paper analyzes in detail (see Fig. 4) the first high-resolution measurement of the $L\gamma_1$ (L_2N_4), $L\gamma_2$ (L_1N_2), $L\gamma_3$ (L_1N_3), and $L\gamma_6$ (L_2O_4) x-ray lines emitted by thorium irradiated with 360-MeV (O^{7+}) oxygen projectiles at the Paul Scherrer Institute in Villigen (Switzerland) [53]. For thorium's $\sim$20 000-eV $L\gamma$ x-ray lines the transmission crystal spectrometer installed in a modified slit DuMond geometry [54] has an energy resolution of $\sim$10 eV. This resolution is sufficient to separate experimentally some M^{-m} satellite $L\gamma$ x-ray lines [53], which correspond to the thorium configurations with m additional holes in the M shell. Moreover, the spectral resolution is high enough to observe, for the first time [53], in the case of Th $L\gamma_6$ x-ray line a N^{-n} satellite structure (which corresponds to the thorium configurations with n additional holes in the N shell).

It is no surprise that the $L\gamma_1, L\gamma_2, L\gamma_3$, and $L\gamma_6$ x-ray spectra for high-Z elements such as thorium (Th, $Z = 90$) and uranium (U, $Z = 92$) are characterized by a very rich structure [53], and that their origin is very difficult to track down. While the $L\gamma_1, L\gamma_2, L\gamma_3$, and $L\gamma_6$ diagram x-ray lines and different M^{-m} satellite x-ray lines may be somewhat separated in energy, they overlap with unresolved satellite structures being the results of ionization of N shell (N^{-n} satellite lines), O shell (O^{-o} satellite lines), and P shell (P^{-p} satellite lines) that, in addition, happen to coincide in energy with L^{-1} hypersatellite structures. Therefore, as has been found in our earlier attempt [45], to reliably decompose the experimental Th $L\gamma$ x-ray spectrum [53] on the theoretical contributions predicted for specific hole configurations, the systematic MCDF study on the various M^{-m}, N^{-n}, and $M^{-m}N^{-n}$ satellite structures should be needed to reproduce all the features visible in $L\gamma_1, L\gamma_2, L\gamma_3$, and $L\gamma_6$ x-ray lines.

II. THEORETICAL BACKGROUND

The methodology of MCDF calculations performed in the present studies is the same as published earlier, in many papers (see, e.g., [5,6,55]). Briefly, the effective Hamiltonian for an N-electron system is expressed by

$$H = \sum_{i=1}^{N} h_D(i) + \sum_{j>i=1}^{N} C_{ij}, \tag{1}$$

where $h_D(i)$ is the Dirac operator for the ith electron and the terms C_{ij} account for electron-electron interactions. The latter are a sum of the Coulomb interaction operator and the transverse Breit operator. An atomic state function (ASF) with the total angular momentum J and parity p is assumed in the form,

$$\Psi_s(J^p) = \sum_m c_m(s)\Phi(\gamma_m J^p), \tag{2}$$

where $\Phi(\gamma_m J^p)$ are configuration state functions (CSF), $c_m(s)$ are the configuration mixing coefficients for state s, and γ_m represents all information required to uniquely define a certain CSF.

The difficulties in estimation of the computational accuracy of *ab initio* methods are discussed in Ref. [51], and with a longer perspective in Ref. [56]. For an assessment of the computational accuracy of our MCDF predictions, in Table II the positions of the $L\gamma_1, L\gamma_2, L\gamma_3$, and $L\gamma_6$ x-ray lines of thorium are compared with the perfect experimental data and theoretical data in the authoritative compilation of Deslattes *et al.* [51] and with experimental Bearden [57] data. For these lines of thorium the measurements [51] are highly accurate, to within 0.06 eV or better, so that the computational accuracy can be gauged by its agreement with the measurements. As can be seen from Table II the accuracy of our predictions for the positions of the $L\gamma_1, L\gamma_2, L\gamma_3$, and $L\gamma_6$ x-ray lines seems to be on the order of 0.4–2.0 eV. Moreover our computations seem to do slightly better than those in Ref. [51]. However, a code's approximation tends to affect the code output the same way, so that the effect or approximations may partly disappear from differences such as energy shifts. Therefore, we can also expect that the precision of our simulations for the satellite and hypersatellite line shapes and positions is even more accurate. Especially, the energy shifts for the $L\gamma_1, L\gamma_2, L\gamma_3$, and $L\gamma_6$ x-ray lines of thorium are much more accurate than absolute line position, i.e., are in the order of 0.1–0.2 eV. To ensure such a high accuracy, it is crucial to use a modified special average-level version of the MCDF method (MCDF-MSAL) [6] and include the two principal QED corrections (self-energy and vacuum polarization), and a finite size nucleus model (with a two-parameter Fermi charge distribution). One demonstration

TABLE II. The energies of the $L\gamma_1, L\gamma_2, L\gamma_3$, and $L\gamma_6$ x-ray diagram lines for Th obtained in our predictions, compared with the theoretical and experimental values in Deslattes *et al.* [51] and experimental values in Bearden [57].

Source	Line positions (eV)			
	$L\gamma_1$	$L\gamma_2$	$L\gamma_3$	$L\gamma_6$
Present	18 981.39	19 302.58	19 505.49	19 600.21
Th. [51]	18 977.6(28)	19 304.5(50)	19 504.3(39)	–
Expt. [51]	18 978.26(2)	19 302.99(5)	19 503.45(6)	–
Expt. [57]	18 982.5	19 305	19 507	19 599

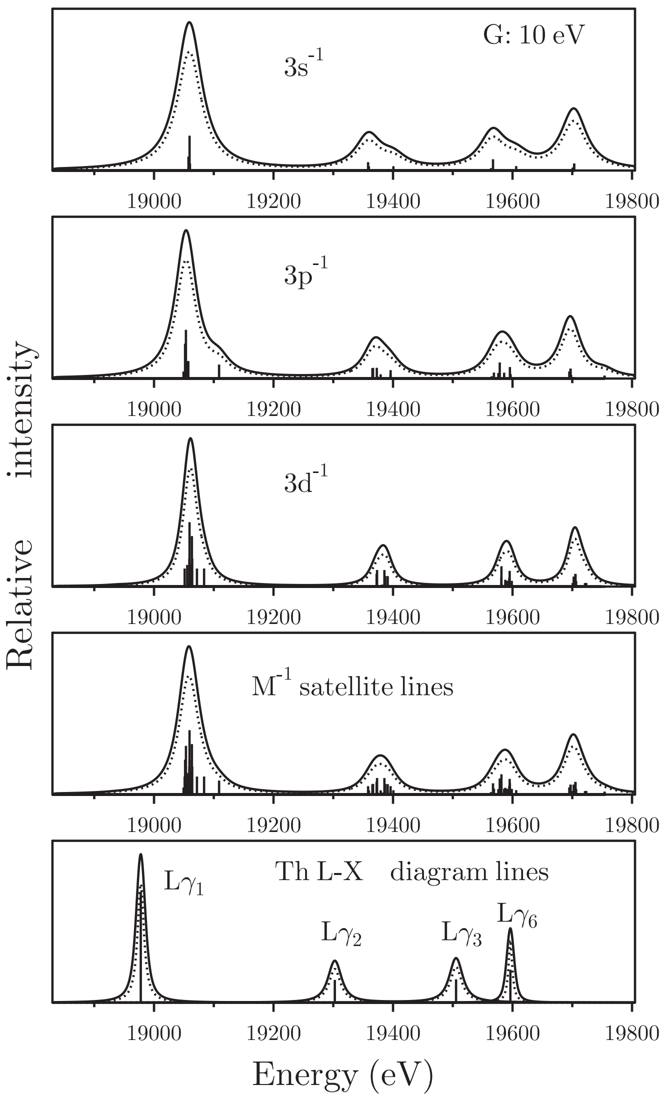

FIG. 1. Calculated spectra for thorium. The sticks give the line positions and their relative intensities. The dashed line is the predicted spectrum, the sum of Lorentzian natural line shapes, and the solid line the convolution of the predicted line shape with the 10-eV Gaussian instrumental response. The bottom spectrum is for the $L\gamma$ diagram transitions, the three top spectra for the individual M satellite transitions. The fourth panel is the sum of the three top spectra.

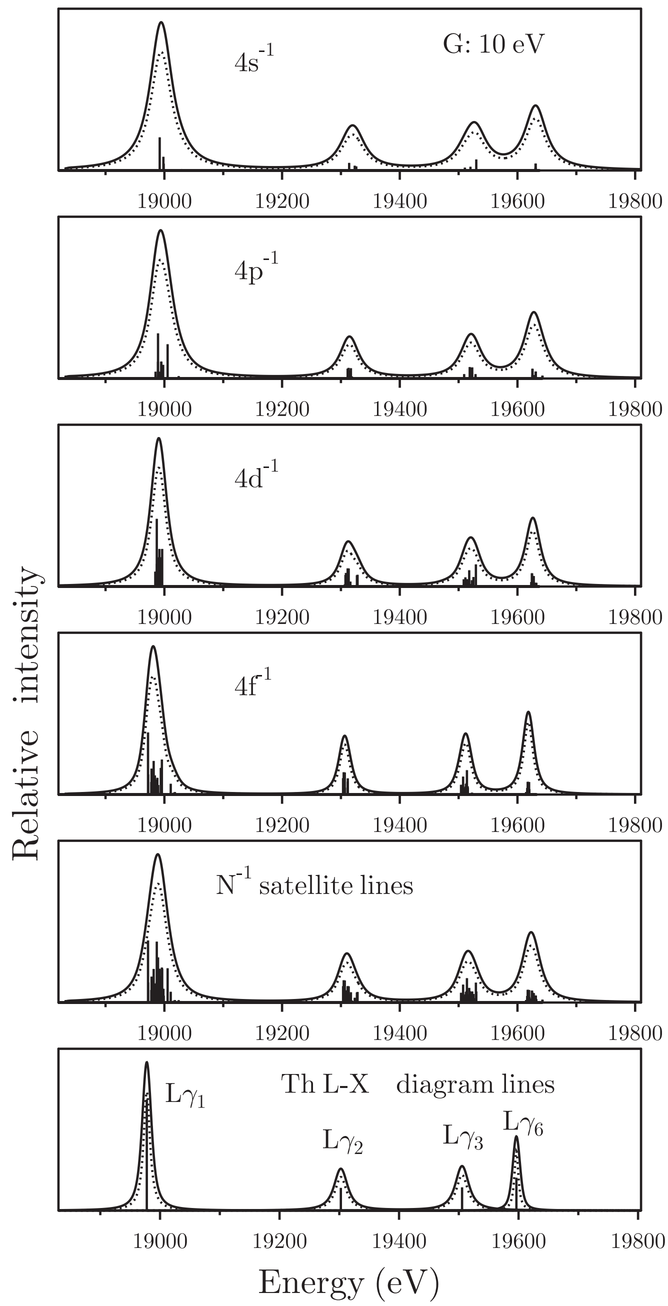

FIG. 2. As in Fig. 1, but for $L\gamma$ diagram transitions (bottom spectrum) and N satellite transitions (five top spectra) for thorium. The fifth panel is the sum of the four top spectra.

of our MCDF method's accuracy is the recent explanation [46] of two K-shell double photoionization mechanisms, shake-off and "knockout," whose relative importance had remained unexplained.

III. PREDICTIONS FOR THE SHAPES AND POSITIONS OF $L\gamma$ X-RAY LINES OF THORIUM

Figures 1–4 reflect the influence of ionization of different shells on the shapes and positions of the $L\gamma_1$ (L_2N_4), $L\gamma_2$ (L_1N_2), $L\gamma_3$ (L_1N_3), and $L\gamma_6$ (L_2O_4) x-ray lines for thorium. Moreover, Tables III–XII give the ionization energy shifts (with respect to the positions of the appropriate diagram lines) for various configurations with the holes in L,M,N,O, and P shells, and for the mixed cases. All tables summarize also the total number of transitions for all studied cases. Especially, in Fig. 4 the predictions of thorium $L\gamma_1, L\gamma_2, L\gamma_3$, and $L\gamma_6$ x-ray line structures have been presented for electronic configurations with one to four vacancies in the M shell with one to three vacancies in the N shell and also for $M^{-1}N^{-1}$, $M^{-1}N^{-2}$, and $M^{-2}N^{-1}$ configurations (see also Table V).

A. Diagram, M^{-1} and N^{-1} satellite, and L^{-1} hypersatellite for thorium $L\gamma$ x-ray lines

As has been mentioned above, we have carried out the detailed predictions of the shapes and positions of thorium $L\gamma_1, L\gamma_2, L\gamma_3$, and $L\gamma_6$ x-ray lines for various configurations

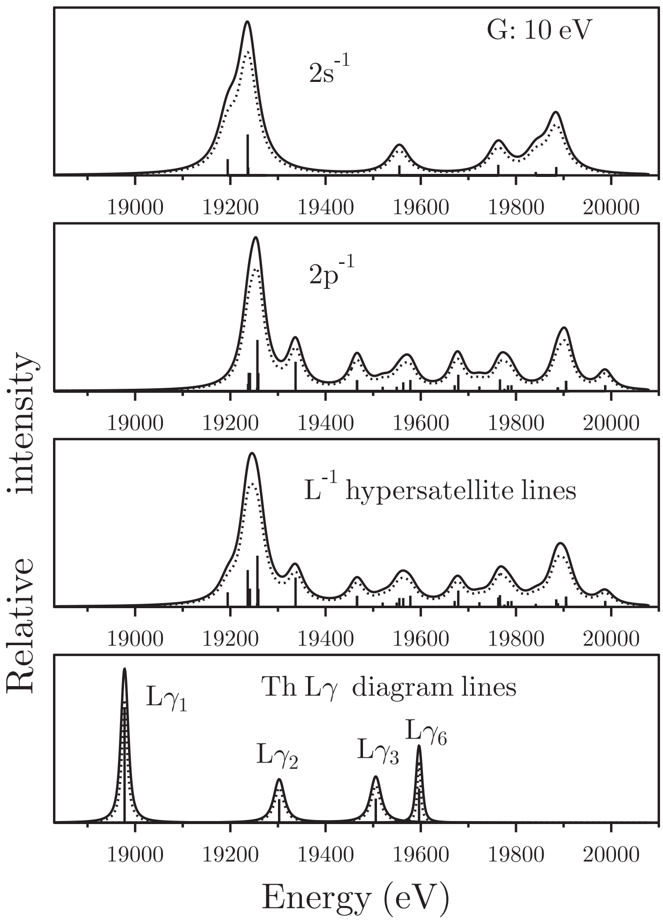

FIG. 3. As in Figs. 1 and 2, but for $L\gamma$ diagram transitions (bottom spectrum) and hypersatellite transitions (three top spectra) for thorium. The third panel is the sum of the two top spectra.

TABLE III. Energy shifts for P^{-1}, O^{-1}, N^{-1}, and M^{-1} satellite $L\gamma$ x-ray lines of thorium.

Hole state	Number of transitions	Energy shift (eV) $L\gamma_1$	$L\gamma_2$	$L\gamma_3$	$L\gamma_6$
$6s^{-1}$	14	0.25	0.14	0.17	1.00
$6p^{-1}$	88	0.39	0.42	0.50	0.96
P^{-1}	102	0.35	0.35	0.42	0.97
$5s^{-1}$	14	1.96	1.35	1.61	8.79
$5p^{-1}$	88	1.92	2.24	2.67	7.74
$5d^{-1}$	103	2.14	1.19	1.32	4.76
O^{-1}	205	2.05	1.56	1.81	6.33
$4s^{-1}$	14	17.4	17.1	19.2	34.5
$4p^{-1}$	72	16.9	11.9	15.4	32.2
$4d^{-1}$	103	12.8	12.6	14.6	29.8
$4f^{-1}$	128	5.95	4.05	6.02	22.2
N^{-1}	317	10.8	8.9	11.0	27.2
$3s^{-1}$	14	81.3	66.8	70.9	106.2
$3p^{-1}$	88	80.4	73.8	77.9	105.0
$3d^{-1}$	126	84.3	79.3	83.5	110.2
M^{-1}	228	82.7	76.1	80.2	108.0

TABLE IV. Energy shifts for L^{-1} hypersatellite $L\gamma$ x-ray lines.

Hole state	Number of transitions	Energy shift (eV) $L\gamma_1$	$L\gamma_2$	$L\gamma_3$	$L\gamma_6$
$2s^{-1}$	10	248.3	252.5	257.3	277.5
$2p^{-1}$	58	290.2	218.8	225.5	320.1
L^{-1}	68	278.3	223.6	230.0	307.9

with the holes in L, M, N, O, and P shells. However, because of the multiplicity and variety of the obtained results for thorium $L\gamma$ x ray we decided to discuss in detail here only the simplest cases, i.e., the predicted structures for M^{-1} satellite lines (see Fig. 1), N^{-1} satellite lines (Fig. 2), and L^{-1} hypersatellite lines (Fig. 3).

In Figs. 1–3 the vertical lines, called "stick spectra," indicate the theoretically computed data for the respective transition: They are located at the energy of the line center, while the height indicates the relative intensity. Moreover, for each type of line are two theoretical spectra of thorium: one (dotted line) being the sum of Lorentzian natural line shapes and the other one (solid line) being the convolution of the sum of Lorentzian natural line shapes with the Gaussian instrumental response (having a width of 10.0 eV [53]) have been predicted.

It is worth noting that in our theoretical predictions for the $L\gamma_1, L\gamma_2, L\gamma_3$, and $L\gamma_6$ x-ray line structures of thorium (Figs. 1–3) the dotted line is the sum of the individual Lorentzian lines, each with its own natural width, and including the ionization effect of N, M, and L shells on the natural linewidths for all individual satellite and hypersatellite lines (see Table I), with data from Campbell and Papp [52].

Figure 1 gives the shapes of the $L\gamma_1, L\gamma_2, L\gamma_3$, and $L\gamma_6$ x-ray lines of thorium that results from ionization of the M shell, separately for each subshell. Removing one electron from the $3s$ subshell produces the top panel marked $3s^{-1}$; the next panel marked $3p^{-1}$ is for single ionization from subshell $3p$,

TABLE V. Energy shifts for L^{-1} hypersatellite $L\gamma$ x-ray lines in comparison to the energy shifts of various satellite lines (with holes in M, N, O, and P shells and mixed hole states).

Hole state	Number of transitions	Energy shift (eV) $L\gamma_1$	$L\gamma_2$	$L\gamma_3$	$L\gamma_6$
P^{-1}	102	0.35	0.35	0.42	0.97
O^{-1}	205	2.05	1.56	1.81	6.33
O^{-2}	1123	–	–	–	12.6
O^{-3}	12 518	–	–	–	19.6
N^{-1}	317	10.8	8.9	11.0	27.2
N^{-2}	17 502	20.1	18.2	22.7	54.7
N^{-3}	662 190	33.4	27.7	35.1	82.8
M^{-1}	228	82.7	76.1	80.2	108.0
$M^{-1}N^{-1}$	26 885	92.5	85.3	94.6	136.1
$M^{-1}N^{-2}$	534 890	102.9	–	–	–
M^{-2}	6296	166.4	153.2	161.5	217.0
$M^{-2}N^{-1}$	306 117	177.9	–	–	–
M^{-3}	99 248	252.2	229.5	246.6	328.1
M^{-4}	539 106	331.6	297.8	334.3	-
L^{-1}	68	278.3	223.6	230.0	307.9

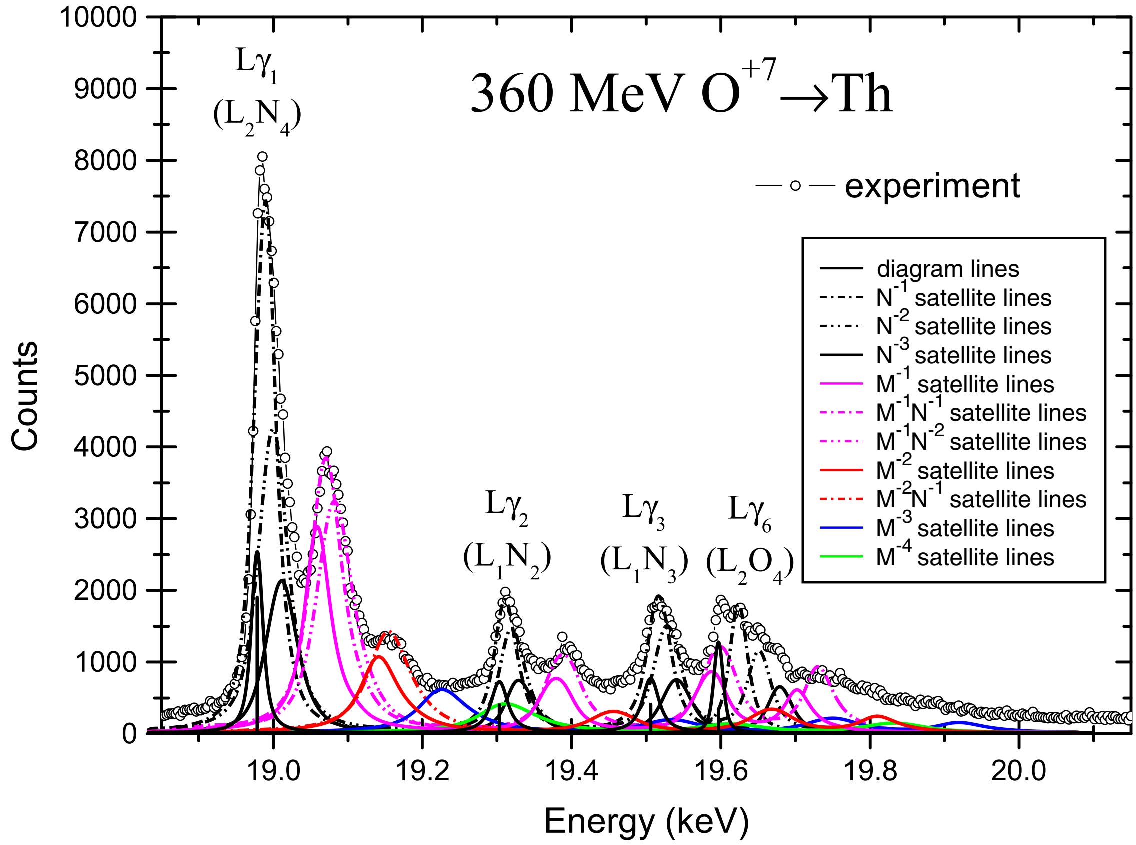

FIG. 4. Comparison of thorium experimental shape for $L\gamma_1, L\gamma_2, L\gamma_3$, and $L\gamma_6$ x-ray spectrum induced by oxygen ions [45,53] with the various theoretically predicted contributions to the spectrum including diagram, M, and N satellite transitions.

and the next one is for single ionization from subshell $3d$. The stick spectra and the resulting shapes of particular satellite $L\gamma$ x-ray lines of thorium clearly depend on the subshell that has been ionized, but in different ways. As an example, ionizing the $3s$ subshell keeps the line shape of the $L\gamma_1$ (L_2N_4) and $L\gamma_6$ (L_2O_4) lines close to Lorentzian, but adds a bump to the high-energy wing of the $L\gamma_2$ and $L\gamma_3$ lines due to a possible transition at a slightly higher energy. In contrast, ionizing from the $3p$ subshell allows an additional transition that modifies the Lorentzian shape of the $L\gamma_1$ line most strongly, but only widens the $L\gamma_2$ and $L\gamma_3$ lines. Table III gives the corresponding data in numerical form. The line shapes in these figures are not qualitatively different for computations that account for hole states in the O and P shells, and for mixed cases when one ionization occurs in the M shell and one or multiple ionizations in the higher shells.

TABLE VI. Energy shifts for N^{-2} and M^{-2} satellite $L\gamma$ lines.

Hole state	Number of transitions	Energy shift (eV)			
		$L\gamma_1$	$L\gamma_2$	$L\gamma_3$	$L\gamma_6$
$4s^{-2}$	4	35.1	35.7	38.8	69.3
$4p^{-2}$	323	34.1	24.5	31.3	64.9
$4d^{-2}$	1127	25.8	25.6	29.5	59.6
$4f^{-2}$	2771	12.0	8.42	12.3	44.5
$4s^{-1}p^{-1}$	257	34.6	29.5	35.1	67.0
$4s^{-1}d^{-1}$	381	30.6	30.2	34.3	64.7
$4s^{-1}f^{-1}$	484	22.9	21.6	25.7	57.2
$4p^{-1}d^{-1}$	2278	29.9	25.0	30.5	62.2
$4p^{-1}f^{-1}$	3248	14.1	16.5	21.9	54.2
$4d^{-1}f^{-1}$	6629	18.8	16.9	20.9	52.3
N^{-2}	17 502	20.1	18.2	22.7	54.7
$3s^{-2}$	4	163.0	133.9	142.8	213.2
$3p^{-2}$	433	161.5	148.9	157.3	211.5
$3d^{-2}$	1521	170.6	159.6	167.3	221.5
$3s^{-1}p^{-1}$	312	162.1	141.4	149.6	212.1
$3s^{-1}d^{-1}$	467	166.3	147.0	155.5	217.4
$3p^{-1}d^{-1}$	3559	165.4	154.3	162.9	215.9
M^{-2}	6296	166.4	153.2	161.5	217.0

Figure 2 presents the influence of ionization of particular subshells of the N shell (i.e., $4s, 4p, 4d$, and $4f$ subshells after removing from them one electron each) on the shapes of $L\gamma_1, L\gamma_2, L\gamma_3$, and $L\gamma_6$ x-ray lines. As is the case of the satellite structures of the M shell (Fig. 1), the structures of stick spectra and predicted shapes of particular $L\gamma$ satellite lines are different for each discussed case. However, these changes are less pronounced than for the satellite structures of the M shell, and the energy shifts of groups of particular satellite lines are less visible than those presented in Fig. 1. The spectra structures from the M shell occur in a ~850 eV wide energy range from about 18 950 eV to about 19 800 eV; those from the N satellite lines occur in a slightly narrower energy range (~810 eV) that is slightly red-shifted to lower energies in addition, from about 18 930 eV to about 19 720 eV as is evident from Table III.

TABLE VII. Energy shifts for N^{-3} and M^{-3} satellite $L\gamma$ lines.

Hole state	Number of transitions	Energy shift (eV) $L\gamma_1$	$L\gamma_2$	$L\gamma_3$	$L\gamma_6$
$4p^{-3}$	509	51.7	37.5	47.7	97.9
$4d^{-3}$	5676	39.2	39.1	44.9	90.2
$4f^{-3}$	30 394	19.1	13.1	18.8	68.0
$4s^{-2}p^{-1}$	72	52.6	48.3	54.8	102.2
$4s^{-2}d^{-1}$	103	48.7	49.1	54.3	100.0
$4s^{-2}f^{-1}$	128	41.9	40.5	45.7	92.6
$4s^{-1}p^{-2}$	1171	52.1	42.3	51.3	100.0
$4s^{-1}d^{-2}$	4252	43.9	43.5	49.6	95.0
$4s^{-1}f^{-2}$	10 675	30.5	26.4	32.5	80.7
$4p^{-2}d^{-1}$	11 268	47.5	37.8	46.6	95.2
$4p^{-2}f^{-1}$	17 317	38.9	24.9	38.1	86.2
$4p^{-1}d^{-2}$	26 419	43.1	38.8	46.1	93.3
$4p^{-1}f^{-2}$	75 833	30.1	20.5	31.3	79.1
$4d^{-2}f^{-1}$	94 181	33.1	30.0	36.4	82.8
$4d^{-1}f^{-2}$	167 436	26.5	22.3	27.6	75.4
$4s^{-1}p^{-1}d^{-1}$	8515	48.0	42.9	50.5	97.5
$4s^{-1}p^{-1}f^{-1}$	12 340	41.0	34.4	41.9	89.9
$4s^{-1}d^{-1}f^{-1}$	25 475	37.1	35.0	40.9	87.9
$4p^{-1}d^{-1}f^{-1}$	170 426	35.8	28.9	38.3	84.5
N^{-3}	662 190	33.4	27.7	35.1	82.8
$3p^{-3}$	749	243.1	224.6	237.1	318.9
$3d^{-3}$	8201	258.3	257.0	263.6	337.3
$3s^{-2}p^{-1}$	88	244.1	208.4	221.7	319.7
$3s^{-2}d^{-1}$	126	240.6	214.5	228.0	315.9
$3s^{-1}p^{-2}$	1639	243.5	216.7	229.2	319.3
$3s^{-1}d^{-2}$	5824	252.5	228.2	241.3	327.2
$3p^{-2}d^{-1}$	20 508	232.8	229.9	245.7	328.0
$3p^{-1}d^{-2}$	48 278	261.2	226.1	249.4	327.8
$3s^{-1}p^{-1}d^{-1}$	13 835	254.8	222.3	235.2	325.2
M^{-3}	99 248	252.2	229.5	246.6	328.1

TABLE VIII. Energy shifts for M^{-4} satellite $L\gamma_1, L\gamma_2$, and $L\gamma_3$ x-ray lines.

Hole state	Number of transitions	Energy shift (eV) $L\gamma_1$	$L\gamma_2$	$L\gamma_3$
$3p^{-4}$	281[a]	325.2	300.9	317.6
$3d^{-4}$	13 616[a]	344.2	325.1	345.9
$3s^{-2}p^{-2}$	281[a]	326.0	284.5	302.0
$3s^{-2}d^{-2}$	959[a]	336.0	296.1	314.2
$3s^{-1}p^{-3}$	1678[a]	325.5	292.9	309.6
$3s^{-1}d^{-3}$	19 637[a]	346.9	313.3	332.1
$3p^{-3}d^{-1}$	20 857[a]	329.8	285.8	321.8
$3p^{-2}d^{-2}$	165 343[a]	319.6	301.4	340.7
$3p^{-1}d^{-3}$	158 670[a]	334.5	288.4	345.3
$3s^{-1}p^{-2}d^{-1}$	45 843[a]	326.2	301.1	325.2
$3s^{-1}p^{-1}d^{-2}$	109 745[a]	334.9	293.0	324.7
$3s^{-2}p^{-1}d^{-1}$	2196[a]	330.7	290.3	308.0
M^{-4}	539 106[a]	331.6	297.8	334.3

[a]Number of transitions calculated for $L\gamma_1, L\gamma_2$, $L\gamma_3$ lines.

TABLE IX. Energy shifts for $M^{-1}N^{-1}$ satellite $L\gamma$ lines.

Hole state	Number of transitions	Energy shift (eV) $L\gamma_1$	$L\gamma_2$	$L\gamma_3$	$L\gamma_6$
$3s^{-1}4s^{-1}$	49	99.1	84.5	90.6	141.3
$3s^{-1}4p^{-1}$	257	98.6	79.3	86.9	139.0
$3s^{-1}4d^{-1}$	381	94.6	80.0	86.3	136.6
$3s^{-1}4f^{-1}$	484	87.7	71.5	77.6	129.3
$3p^{-1}4s^{-1}$	312	98.2	91.5	97.8	140.1
$3p^{-1}4p^{-1}$	1822	97.9	86.5	94.1	137.9
$3p^{-1}4d^{-1}$	2846	93.6	87.2	93.4	134.2
$3p^{-1}4f^{-1}$	3750	86.5	78.7	84.9	126.5
$3d^{-1}4s^{-1}$	467	102.1	97.0	103.5	145.2
$3d^{-1}4p^{-1}$	2927	101.8	91.8	99.7	142.8
$3d^{-1}4d^{-1}$	5381	98.1	92.7	97.0	141.8
$3d^{-1}4f^{-1}$	8209	85.4	84.9	100.3	135.0
$M^{-1}N^{-1}$	26 885	92.5	85.3	94.6	136.1

Table III gives the numerical values of the energy shifts for the $L\gamma_1, L\gamma_2, L\gamma_3$, and $L\gamma_6$ satellite x-ray lines. They summarize the situation with one hole in a particular subshell of M, N, O, and P shells. The data in Table III show that ionization of the various subshells affects the different $L\gamma$ x-ray line differently. The largest energy shifts occur after removing an electron from the M subshells. The average energy shifts resulting from deletion of the singular electron from the M shell for particular types of $L\gamma$ x-ray lines are, respectively, as follows: 76.1 eV for the $L\gamma_2$ line; 80.2 eV for the $L\gamma_3$ line; 82.7 eV for the $L\gamma_1$ line; and 108.0 eV for the $L\gamma_6$ line (see the last row of Table III). The largest energy shifts after removing an electron from the M shell have been noted for the 3d subshell. Much smaller average energy shifts occur after removing an electron from the N shell. Their average values are within the limits from 8.9 eV for the $L\gamma_2$ line to 27.2 eV for the $L\gamma_6$ line. The highest values of energy shifts for

TABLE X. Energy shifts O^{-2} and O^{-3} satellite $L\gamma_6$ lines.

Hole state	Number of transitions	Energy shift (eV) $L\gamma_6$
$5s^{-2}$	1[a]	17.8
$5p^{-2}$	144[a]	15.6
$5d^{-2}$	168[a]	9.27
$5s^{-1}p^{-1}$	105[a]	16.8
$5s^{-1}d^{-1}$	82[a]	13.8
$5p^{-1}d^{-1}$	623[a]	12.5
O^{-2}	1123[a]	12.6
$5p^{-3}$	237[a]	23.9
$5d^{-3}$	613[a]	14.2
$5s^{-2}p^{-1}$	29[a]	61.2
$5s^{-2}d^{-1}$	22[a]	23.2
$5s^{-1}p^{-2}$	525[a]	24.9
$5s^{-1}d^{-2}$	634[a]	18.7
$5p^{-2}d^{-1}$	3263[a]	20.7
$5p^{-1}d^{-2}$	4918[a]	17.4
$5s^{-1}p^{-1}d^{-1}$	2277[a]	21.7
O^{-3}	12 518[a]	19.6

[a]Number of transitions calculated only for the $L\gamma_6$ x-ray line.

TABLE XI. Energy shifts for $M^{-1}N^{-2}$ satellite $L\gamma_1$ lines.

Hole state	Number of transitions	Energy shift (eV) $L\gamma_1$
$3s^{-1}4s^{-2}$	4[a]	117.0
$3s^{-1}4p^{-2}$	525[a]	116.1
$3s^{-1}4d^{-2}$	661[a]	107.9
$3s^{-1}4f^{-2}$	4050[a]	94.9
$3s^{-1}4s^{-1}p^{-1}$	381[a]	116.5
$3s^{-1}4s^{-1}d^{-1}$	305[a]	112.6
$3s^{-1}4s^{-1}f^{-1}$	673[a]	105.8
$3s^{-1}4p^{-1}d^{-1}$	2302[a]	110.9
$3s^{-1}4p^{-1}f^{-1}$	5447[a]	105.7
$3s^{-1}4d^{-1}f^{-1}$	5628[a]	100.8
$3p^{-1}4s^{-2}$	29[a]	116.2
$3p^{-1}4p^{-2}$	3806[a]	115.2
$3p^{-1}4d^{-2}$	5015[a]	84.4
$3p^{-1}4f^{-2}$	34 456[a]	93.5
$3p^{-1}4s^{-1}p^{-1}$	2675[a]	116.8
$3p^{-1}4s^{-1}d^{-1}$	2303[a]	125.9
$3p^{-1}4s^{-1}f^{-1}$	5535[a]	102.0
$3p^{-1}4p^{-1}d^{-1}$	17 390[a]	113.8
$3p^{-1}4p^{-1}f^{-1}$	43 168[a]	99.0
$3p^{-1}4d^{-1}f^{-1}$	46 290[a]	87.1
$3d^{-1}4s^{-2}$	45[a]	112.4
$3d^{-1}4p^{-2}$	6753[a]	123.8
$3d^{-1}4d^{-2}$	10 191[a]	108.5
$3d^{-1}4f^{-2}$	78 693[a]	95.8
$3d^{-1}4s^{-1}p^{-1}$	4706[a]	118.8
$3d^{-1}4s^{-1}d^{-1}$	4476[a]	115.4
$3d^{-1}4s^{-1}f^{-1}$	11 992[a]	108.9
$3d^{-1}4p^{-1}d^{-1}$	34 762[a]	118.0
$3d^{-1}4p^{-1}f^{-1}$	97 700[a]	101.9
$3d^{-1}4d^{-1}f^{-1}$	104 929[a]	104.6
$M^{-1}N^{-2}$	534 890[a]	102.9

[a]Number of transition calculated only for $L\gamma_1$ x-ray line.

TABLE XII. Energy shifts for $M^{-2}N^{-1}$ satellite $L\gamma_1$ lines.

Hole state	Number of transitions	Energy shift (eV) $L\gamma_1$
$3s^{-2}4s^{-1}$	4[a]	180.9
$3s^{-2}4p^{-1}$	29[a]	180.6
$3s^{-2}4d^{-1}$	22[a]	176.7
$3s^{-2}4f^{-1}$	46[a]	169.9
$3s^{-1}p^{-1}4s^{-1}$	381[a]	180.1
$3s^{-1}p^{-1}4p^{-1}$	2663[a]	179.8
$3s^{-1}p^{-1}4d^{-1}$	2302[a]	175.5
$3s^{-1}p^{-1}4f^{-1}$	5581[a]	174.8
$3s^{-1}d^{-1}4s^{-1}$	627[a]	184.3
$3s^{-1}d^{-1}4p^{-1}$	4741[a]	184.6
$3s^{-1}d^{-1}4d^{-1}$	4451[a]	180.4
$3s^{-1}d^{-1}4f^{-1}$	12 097[a]	171.3
$3p^{-1}d^{-1}4s^{-1}$	4675[a]	183.7
$3p^{-1}d^{-1}4p^{-1}$	35 672[a]	184.7
$3p^{-1}d^{-1}4d^{-1}$	35 091[a]	180.8
$3p^{-1}d^{-1}4f^{-1}$	96 966[a]	144.7
$3p^{-2}4s^{-1}$	554[a]	179.5
$3p^{-2}4p^{-1}$	3946[a]	179.0
$3p^{-2}4d^{-1}$	3445[a]	161.2
$3p^{-2}4f^{-1}$	8457[a]	145.4
$3d^{-2}4s^{-1}$	2114[a]	187.9
$3d^{-2}4p^{-1}$	16 638[a]	190.7
$3d^{-2}4d^{-1}$	16 482[a]	182.3
$3d^{-2}4f^{-1}$	49 133[a]	177.4
$M^{-2}N^{-1}$	306 117[a]	177.9

[a]Number of transitions calculated only for the $L\gamma_1$ x-ray line.

the N shell have been observed in the case of electron removal from the $4s$ subshell. About five-times-lower values of average energy shifts occur for the O shell. In the case of removing an electron from the P shell the energy shifts are small and do not exceed 1 eV. Table III also summarizes the total number of transitions for $L\gamma$ x-ray lines resulting from the removal of one electron from each subshell and the summary numbers of transitions for M,N,O, and P shells, from which one electron has been removed.

The detailed analysis of a thorium's hypersatellite $L\gamma_1,L\gamma_2,L\gamma_3$, and $L\gamma_6$ x-ray line structures (i.e., for electronic configurations with one hole in the L shell) has been prepared analogously as for satellite transitions. Therefore, the theoretical stick spectra (line positions with their relative intensities) for hypersatellite $L\gamma$ x-ray lines have been simulated. Moreover, for each type of $L\gamma$ x-ray line there are two theoretically predicted spectra: one being the sum of Lorentzian natural line shapes [52] and the other one being the convolution of the sum of Lorentzian natural line shapes with the Gaussian instrumental response (see Fig. 3). In the case of thorium hypersatellite transitions the x-ray spectra structures are much more complex than for the satellite transitions. While the removal of one electron from the $2s$ subshell does not affect the formation of complex spectra structures, the structures are more complicated and radically shifted with respect to diagram lines. The removal of one electron from the $2p$ subshell for all four analyzed $L\gamma$ x-ray lines gives complex and irregular structures, difficult to separate into individual contributions. It is noteworthy that the hypersatellite structures of $L\gamma_1,L\gamma_2,L\gamma_3$, and $L\gamma_6$ x-ray lines for thorium are distributed in the energy range of about 19 000 eV to about 20 030 eV (see Fig. 3).

The number of transition and values of energy shifts for Th hypersatellite $L\gamma$ x-ray lines have been presented in Table IV. The values shown in the last row (for L^1 hole state) represent the total number of transitions and the average values of energy shifts for particular $L\gamma$ x-ray lines. In Table V we have been presented the values of energy shifts for hypersatellite $L\gamma$ x-ray lines of thorium (the values collected in the last row, L^{-1}, indicating the hole in the L shell) and, for comparison, the values of energy shifts achieved for satellite $L\gamma$ x-ray lines of thorium (with the holes in the M,N,O, and P shells and mixed hole states). As can be seen in all cases of particular shell ionizations the energy shifts are dependent strongly on the kind of $L\gamma$ x-ray lines, i.e., they are different for $L\gamma_1,L\gamma_2,L\gamma_3$, and $L\gamma_6$ lines. The largest energy shifts have been found for hypersatellite x-ray structures, i.e., 278.3 eV for $L\gamma_1$, 223.6 eV for $L\gamma_2$, 230.0 eV for $L\gamma_3$, and 307.9 eV for $L\gamma_6$ x-ray lines. The energy shifts of presented satellite structures (with one hole in the M,N,O or P shell) are much smaller and for all types of x-ray lines are in the range of

0.35 eV for the hole in the P shell to 108.0 eV for the hole in the M shell. Among the hypersatellite x-ray lines, the most shifted towards higher energies are those of the $L\gamma_6$ x-ray lines. This regularity also can be seen in the case of satellite x-ray lines. Much more detailed discussion of our results obtained for the $L\gamma_1, L\gamma_2, L\gamma_3$, and $L\gamma_6$ satellite lines for various hole configurations, being an effect of multiple ionization of particular subshells for M, N, and O shells and also mixed hole states, is presented in the Appendix.

B. Unraveling the origin of complex structure of Th $L\gamma$ x-ray lines in registered high-resolution spectra

As mentioned in Sec. I, the most important motivation for realization of extensive theoretical study presented in this paper was to enable a quantitative interpretation of the high-resolution $L\gamma$ x-ray spectrum of thorium induced by 360 and 230 MeV oxygen projectiles [53]. The only systematic way to do this is to predict the spectra for the hole configurations to be expected from multiply-ionized thorium, and then use these spectra to match the measured spectrum. Since specific hole states may be correlated with the emission of a particular $L\gamma$ x-ray line, the measured spectrum does not necessarily correspond to a particular ionization state, hence it is best to start by comparing the computed spectra with the individual features in the measured spectrum.

Figure 4 presents the comparison of thorium experimental shape for $L\gamma_1, L\gamma_2, L\gamma_3$, and $L\gamma_6$ x-ray spectrum induced by oxygen ions (in the open circles) [45,53] with the various theoretically predicted contributions to the spectrum including all diagram, and various M^{-m}, N^{-n}, and $M^{-m}N^{-n}$ satellite lines (see the legend). Only a detailed comparison of the particular peak positions and shapes of the experimental spectrum with the results of theoretical predictions for individual electronic configurations (for $L\gamma_1, L\gamma_2, L\gamma_3$, and $L\gamma_6$ x-ray lines) allow one to explain fully the extremely complex origin of the registered spectrum. For better visualization the particular contributions of the predicted spectrum in Fig. 4 have amplitudes defined by the best match to the lines in which they dominate. The theoretical black lines with the stick spectra inside are the diagram transitions as in the bottom panels of Figs. 1–3. We can see that the experimental spectrum has the corresponding lines as well but shifted to slightly higher energies. The colored solid lines correspond to the pure M^{-m} satellite lines, i.e., without additional holes in the N shell, as follows: M^{-1} (magenta line), M^{-2} (red line), M^{-3} (blue line), and M^{-4} (green line).

As can be easily seen from Fig. 4, only for the $L\gamma_1$ x-ray line the structures of diagram, N^{-n} satellite ($n = 1, 2, 3$), $M^{-1}N^{-n}$ satellite ($n = 0, 1, 2$), and $M^{-2}N^{-n}$ satellite ($n = 0, 1$) lines are not disrupted by the other $L\gamma$ lines, i.e., by $L\gamma_2, L\gamma_3, L\gamma_6$ lines. This is the result of the fact that the $L\gamma_2, L\gamma_3, L\gamma_6$ lines are not covering this part of $L\gamma_1$ line structures. The $L\gamma_2$ diagram and N^{-n} satellite, and M^{-m} satellite lines are partially covered by the $L\gamma_1$ line because of the overlap with M^{-3} and M^{-4} satellites of the $L\gamma_1$ line. Also the $L\gamma_3$ diagram and N^{-n} satellite lines are covered, but by the $L\gamma_2$ line because of the overlap with M^{-2} and M^{-3} satellites of this line. An especially complicated situation is for the $L\gamma_6$ diagram and satellite lines. The $L\gamma_6$ diagram and N^{-n} satellite, and M^{-1} and M^{-2} satellite lines are covered by the overlap with M^{-1} and M^{-2} satellites of the $L\gamma_3$ line. Moreover, it is worth noting that the influence of $L\gamma_1$ hypersatellite lines on the structures of $L\gamma_2, L\gamma_3$, and $L\gamma_6$ lines should be taken into account, because of their overlapping.

However, the best match to three of the five main experimental $L\gamma$ peaks, in particular for the highest-intensity $L\gamma_1$ (L_2N_4) x-ray line at about 19 000 eV and for $L\gamma_2$ and $L\gamma_3$ x-ray lines, comes from the predicted N^{-1} satellite structures, for transitions with one additional hole in the N shell as shown in the black dash-dot line. The exception is the complicated structure around the $L\gamma_6$ line, where the corresponding transitions in the N^{-1} satellite spectrum are an excellent match to a slightly smaller second peak in this line's complicated structure. In a future attempt to represent the measured spectrum (region at about 19 670 eV) by the predicted N^{-n} satellite structures of the $L\gamma_6$ line, a significant contribution comes from the N^{-2} satellite spectrum, for configurations with two vacancies (black dash-dot-dot line), and the N^{-3} satellite spectrum, and three vacancies (black dash-dot-dot-dot line) in the N shell.

In the registered spectrum the peak at 19 090 eV is clearly from the M^{-1} satellite of the $L\gamma_1$ x-ray line, with an ~90 eV blueshift that matches the $L\gamma$ spectrum predicted for an electron removing from the M shell, the magenta lines. The best match is for the $M^{-1}N^{-1}$ satellite spectrum (magenta dash-dot line), while the satellite spectrum $M^{-2}N^{-1}$ (red dash-dot line) for Th ions with two electrons removed from the M shell and one from the N shell may well be responsible for the smaller feature at 19 180 eV.

The lower-intensity $L\gamma_2$ x-ray line (L_1N_2 transitions) at 19 300 eV shows features that are qualitatively similar to those for the $L\gamma_1$ x-ray line: It is blue-shifted by ~15 eV as computed for the N^{-1} satellite spectrum (black dash-dot line), and at ~80 eV more a peak that corresponds to the $M^{-1}N^{-1}$ satellite spectrum (magenta dash-dot line). A hint of the M^{-2} spectrum (red solid line) may be visible at 19 450 eV, but for still higher energies the $L\gamma_2$ runs into the $L\gamma_3$ line whose composition is in terms of satellite lines. However, the lower-energy peak at 19 600 eV of the complicated feature identified in Fig. 4 as the $L\gamma_6$ line corresponds to the $L\gamma_3$ line for the M^{-2} satellite spectrum while the small peak at slightly higher energy may well be from the $L\gamma_6$ line in the N^{-1} satellite spectrum. Moreover, we can see that the N^{-2} and N^{-3} satellites of $L\gamma_6$ x-ray lines properly reproduce details of the spectrum feature in the region 19 650–19 700 eV.

Based on the analysis of Fig. 4 one can see that each detail (every sharp and other peaks) observed on the $L\gamma$ high-resolution spectrum of thorium can be assigned to the particular type of configurations for thorium ions. Moreover, it is worth noting that these details (peaks) for both diagram and M^{-1} (and M^{-2} for $L\gamma_1$) satellite lines correspond evidently to the configuration types with one additional hole in the N shell. However, in the case of the $L\gamma_6$ line these details can be assigned to the configuration types with one, two and three holes in the N shell.

The excellent match between the energies of the visible peaks in this high-resolution spectrum of thorium suggests that the predicted contributions to the spectrum have been done with a very high accuracy, and that such systematic theoretical

MCDF calculations are extremely useful to get a grip on such a complex high-resolution spectrum. Furthermore, the detailed comparison of the experimental $L\gamma$ x-ray spectrum with the results of predicted spectra of thorium presented in Fig. 4 indicates that reliable interpretation of such a complex high-resolution spectrum would be impossible without the systematical theoretical predictions as presented in this paper. However, to determine a representative ionization state for thorium in such experiments from the x-ray spectra, further work must be done.

IV. SUMMARY AND CONCLUSIONS

The reliable quantitative interpretation of high-resolution structures of $L\gamma_1, L\gamma_2, L\gamma_3$, and $L\gamma_6$ x-ray lines of the thorium spectrum induced by 230 and 360 MeV oxygen projectiles [53] has not been performed until now because of their complex origin [45] being the result of multiple ionizations of various shells of target atoms in collisions with heavy ions. Moreover, the complexity of these structure origins, for the studied range of the measured spectrum is caused by the additional effect, i.e., the strong overlapping of each contribution of various satellite (and hypersatellite) structures of $L\gamma_1, L\gamma_2, L\gamma_3$, and $L\gamma_6$ x-ray lines (see Fig. 4). Therefore, in this paper we present the results of our systematic and sophisticated, performed for many years, MCDF study concerning the very complicated structure of the diagram, different N^{-n} and M^{-m} satellites, and also L^{-1} hypersatellite $L\gamma$ x-ray lines of thorium (Tables III–XII and Figs. 1–4).

As already has been found in Sec. III (see Fig. 4), each detail observed on the high-resolution $L\gamma$ x-ray spectrum of thorium induced by 360-MeV oxygen projectiles can be assigned to the particular type of thorium ion configurations. Moreover, evidently these details for both the $L\gamma_1, L\gamma_2, L\gamma_3$, and $L\gamma_6$ diagram x-ray lines and M^{-1} (and M^{-2} for $L\gamma_1$) satellite x-ray lines correspond evidently to the configuration types with one additional hole in the N shell. In the case of the $L\gamma_6$ line these details can be assigned to the configuration types with one, two, and three holes in the N shell. Therefore, we can definitely conclude that the extraordinary precision of position and shape reproduction of all details for characteristic parts of the high-resolution $L\gamma$ x-ray spectrum of thorium induced by oxygen projectiles fully confirms the very high accuracy of our systematical MCDF predictions.

The results of our systematic study presented in this paper, allowed us to unravel the complex origin (and overlapping) structure of $L\gamma_1, L\gamma_2, L\gamma_3$, and $L\gamma_6$ x-ray lines of thorium in high-resolution spectra induced by heavy projectiles. Moreover, our results are the precursor for proper quantitative interpretation of the structures of $L\gamma_1, L\gamma_2, L\gamma_3$, and $L\gamma_6$ lines in high-resolution x-ray spectra of thorium induced in collision with 360-MeV (presented in Fig. 4), and with 230-MeV oxygen ions [53], and also other thorium $L\gamma$ x-ray spectra induced by light and heavy projectiles.

We would like to emphasize that the reliable decomposition of high-resolution $L\gamma$ x-ray spectra of thorium, such as presented in Fig. 4, seems to be possible in the near future, on the basis of data shown here, in a similar but more complicated procedure as was performed and presented recently in the series of articles by Czarnota *et al.* [42–44]. It should be noted that we already start to develop the more general and universal procedure, and the special dedicated numerical program package, which can allow one to make such decomposition.

Moreover, we believe that the results of research presented in this article should be not only the valuable basis for interpretation of the thorium $L\gamma$ x-ray spectrum induced by different light and heavy projectiles (by decomposition on theoretical contribution) but also can be very helpful in planning new measurements of $L\gamma$ x-ray spectra of heavy elements produced in different light and heavy projectiles.

ACKNOWLEDGMENTS

This work is supported by the Polish National Science Center under Grant No. 2011/01/D/ST2/01286. We thank Nino R. Pereira for editorial suggestions that improved the readability of the paper.

APPENDIX

The extensive data of transition amounts and energy shifts created from the thorium configuration changes after removing more than one electron from particular subshells in the case of M, N, and O shells for $L\gamma_1, L\gamma_2, L\gamma_3$, and $L\gamma_6$ x-ray lines have been collected in Tables VI–XII. These tables present the detailed calculation results for thorium different configurations after eliminating two and three electrons from M and N shells (see in Tables VI and VII), and simultaneously removing one electron from both M and N shells (see in Table IX) for $L\gamma_1, L\gamma_2, L\gamma_3$, and $L\gamma_6$ x-ray lines. Moreover, there are collected the calculation results for four holes in the M shell for $L\gamma_1, L\gamma_2$, and $L\gamma_3$ x-ray lines (see in Table VIII), and two and three holes in the O shell for the $L\gamma_6$ x-ray line (see in Table X). Additionally, one has presented the results for $M^{-1}N^{-2}$ and $M^{-2}N^{-1}$ hole cases of the $L\gamma_1$ x-ray line for the discussed chemical element (see Tables XI and XII).

After detailed analysis of Tables VI–XII for thorium, one can conclude that additional ionizations in the O shell influence in a small way the energy shifts of the satellite $L\gamma_6$ x-ray line, i.e., the average energy shift for the O^2 hole state is about 12.6 eV, whereas for the O^{-3} hole state – 19.6 eV (see Table X). Additional ionization of the N shell affects on average energy shifts from the range of 18.2 eV for $L\gamma_2$ to 54.7 eV for $L\gamma_6$ x-ray lines after simultaneously removing two electrons from the N shell (see Table VI) and from the range of 27.7 eV for $L\gamma_2$ to about 82.8 eV for $L\gamma_6$ x-ray lines after simultaneously removing three electrons from the N shell (see Table VII).

In the case of mixed hole states ($M^{-1}N^{-1}, M^{-1}N^{-2}$, and $M^{-2}N^{-1}$) the values of energy shifts are not remarkably large, though of course significantly higher than for the previously discussed multivacancy cases. For the $M^{-1}N^{-1}$ hole state the average energy shifts are equal, respectively: 85.3 eV for $L\gamma_2$, 92.5 eV for $L\gamma_1$, 94.6 eV for $L\gamma_3$, and 136.1 eV for the $L\gamma_6$ x-ray lines (see Table IX). Whereas the calculated values of average energy shifts for the $M^{-1}N^{-2}$ and $M^{-2}N^{-1}$ hole states are for the $L\gamma_1$ x-ray line equal, respectively: 102.9 eV after simultaneously removing one electron from the M shell and two electrons from the N shell (see Table XI) and 177.9 eV after simultaneously removing two electrons from the M shell and one electron from the N shell (see Table XII).

Finally, the largest effects of the configuration changes in the thorium atom always occur for an additional ionization of the M shell. For the M^{-2} hole state (after removing two electrons from the M shell) the average energy shifts vary in the range of 153.2 eV for $L\gamma_2$ to 217.0 eV for $L\gamma_6$ x-ray lines (see Table VI). The average effect of energy shifts is larger for M^{-3} hole state and equals from 229.5 eV for $L\gamma_2$ to 328.1 eV for $L\gamma_6$ x-ray lines of thorium (see Table VII). Therefore as can be concluded, the largest energy shifts are present after simultaneously removing four electrons from the M shell. Then these average values are equal, respectively: 297.8 eV for $L\gamma_2$, 331.6 eV for $L\gamma_1$, and 334.3 eV for $L\gamma_3$ x-ray lines of thorium (the calculations have not been prepared in this case for the $L\gamma_6$ x-ray line; see Table VIII).

For the discussed four types of $L\gamma$ x-ray lines the effect of the smallest energy shifts for analyzed hole states is observed predominantly for the $L\gamma_2$ x-ray line, while the largest energy shifts can be typically seen for the $L\gamma_6$ x-ray line of thorium. The presented particular numeric cases have been investigated in the MCDF calculations because they all were necessary to carry out precise and reliable analysis of the experimental $L\gamma$ x-ray spectrum of thorium, and then its separation into individual contributions.

Moreover, it is worth emphasizing that the additional ionization of the thorium atom not only affects the formation of complex $L\gamma$ x-ray spectra structures and significant values of energy shifts for particular x-ray lines, but results from the huge number of transitions which accompany these complex cases. For analyzed $L\gamma$ x-ray lines of thorium the largest number of transitions has been observed for the $4p^{-1}d^{-1}f^{-1}$ hole state (after simultaneously removing one electron from the $4p$ subshell, one from the $4d$ subshell, and one from the $4f$ subshell) and it was equal up to 170 426. The largest total number of transitions has been observed for the case of three holes in the N shell (N^{-3}). The number of transitions in this case was 662 190, reflecting the enormous complexity of analyzed $L\gamma$ x-ray spectra for thorium.

[1] S. N. Nahar, A. K. Pradhan, and C. Sur, J. Quant. Spectrosc. Radiat. Transfer **109**, 1951 (2008).
[2] R. L. Watson, V. Horvat, and Y. Peng, Phys. Rev. A **78**, 062702 (2008).
[3] R. Diamant, S. Huotari, K. Hämäläinen, R. Sharon, C. C. Kao, and M. Deutsch, Phys. Rev. A **79**, 062511 (2009).
[4] R. Diamant, S. Huotari, K. Hämäläinen, R. Sharon, C. C. Kao, V. Honkimäki, T. Buslaps, and M. Deutsch, Phys. Rev. A **79**, 062512 (2009).
[5] M. Polasik, Phys. Rev. A **39**, 616 (1989); **39**, 5092 (1989); **40**, 4361 (1989); **41**, 3689 (1990).
[6] M. Polasik, Phys. Rev. A **52**, 227 (1995).
[7] M. Polasik and M. Lewandowska-Robak, J. Phys. B **39**, 1169 (2006).
[8] M. Polasik and M. Lewandowska-Robak, Phys. Rev. A **70**, 052502 (2004).
[9] M. Czarnota, M. Pajek, D. Banaś, D. Chmielewska, J. Rzadkiewicz, Z. Sujkowski, J.-Cl. Dousse, M. Berset, O. Mauron, Y.-P. Maillard, P. A. Raboud, J. Hoszowska, M. Polasik, and K. Słabkowska, Nucl. Instr. Meth. Phys. Res. B **205**, 133 (2003).
[10] K. Fennane, M. Berset, J.-Cl. Dousse, J. Hoszowska, P.-A. Raboud, and J. L. Campbell, Phys. Rev. A **88**, 052506 (2013).
[11] Y. Özdemir, R. Durak, K. Esmer, and M. Ertuğrul, J. Quant. Spectrosc. Radiat. Transfer **90**, 161 (2005).
[12] H. V. Rahangdale, D. Mitra, P. K. Das, S. De, M. Guerra, J. P. Santos, and S. Saha, J. Quant. Spectrosc. Radiat. Transfer **174**, 79 (2016).
[13] Y. Özdemir, J. Quant. Spectrosc. Radiat. Transfer **83**, 295 (2004).
[14] M. R. Kacal, I. Han, F. Akman, and R. Durak, J. Quant. Spectrosc. Radiat. Transfer **113**, 373 (2012).
[15] Y.-P. Maillard, J.-Cl. Dousse, and J. Hoszowska, Eur. Phys. J. D **57**, 155 (2010).
[16] Y. Wu, Z. An, Y. M. Duan, and M. T. Liu, J. Phys. B: At. Mol. Opt. Phys. **43**, 135206 (2010).
[17] H. V. Rahangdale, M. Guerra, P. K. Das, S. De, J. P. Santos, D. Mitra, and S. Saha, Phys. Rev. A **89**, 052708 (2014).
[18] G. Lapicki, A. C. Mandal, S. Santra, D. Mitra, M. Sarkar, D. Bhattacharya, P. Sen, L. Sarkadi, and D. Trautmann, Phys. Rev. A **72**, 022729 (2005).
[19] Y. Wu, Z. An, Y. M. Duan, M. T. Liu, and C. H. Tang, J. Phys. B: At. Mol. Opt. Phys. **40**, 735 (2007).
[20] A. Kumar, Y. Chauhan, and S. Puri, At. Data Nucl. Data Tables **96**, 567 (2010).
[21] I. Han, L. Demir, and M. Ağbaba, Radiat. Phys. Chem. **76**, 1551 (2007).
[22] Ö. Söğüt, G. Apaydın, Ö. Şimşek, E. Cengiz, M. Saydam, N. Küp, and E. Tíraşoğlu, Radiat. Phys. Chem. **78**, 307 (2009).
[23] K. Słabkowska and M. Polasik, Radiat. Phys. Chem. **75**, 1471 (2006).
[24] K. Słabkowska and M. Polasik, J. Phys.: Conf. Ser. **58**, 263 (2007).
[25] G. Kaur and R. Mittal, J. Quant. Spectrosc. Radiat. Transfer **133**, 489 (2014).
[26] H. Hou and F. Kong, J. Quant. Spectrosc. Radiat. Transfer **111**, 2505 (2010).
[27] A. Moy, C. Merlet, X. Llovet, and O. Dugne, J. Phys. B: At. Mol. Opt. Phys. **46**, 115202 (2013).
[28] A. Moy, C. Merlet, X. Llovet, and O. Dugne, J. Phys. B: At. Mol. Opt. Phys. **47**, 055202 (2014).
[29] M. Polasik and K. Słabkowska, Radiat. Phys. Chem. **75**, 1497 (2006).
[30] S. P. Limandri, J. C. Trincavelli, R. D. Bonetto, and A. C. Carreras, Phys. Rev. A **78**, 022518 (2008).
[31] P. Matuszak, K. Kozioł, M. Polasik, and K. Słabkowska, J. Phys.: Conf. Ser. **163**, 012049 (2009).

[32] S. N. Nahar and A. K. Pradhan, J. Quant. Spectrosc. Radiat. Transfer **155**, 32 (2015).
[33] L. V. Skripnikov and A. V. Titov, Phys. Rev. A **91**, 042504 (2015).
[34] Z. Hu, X. Han, Y. Li, D. Kato, X. Tong, and N. Nakamura, Phys. Rev. Lett. **108**, 073002 (2012).
[35] M. S. Pindzola, J. Phys. B: At. Mol. Opt. Phys. **48**, 015201 (2015).
[36] M. S. Pindzola, Phys. Rev. A **90**, 022708 (2014).
[37] A. K. Pradhan, S. N. Nahar, M. Montenegro, Y. Yu, H. L. Zhang, C. Sur, M. Mrozik, and R. M. Pitzer, J. Phys. Chem. A **113**, 12356 (2009).
[38] M. Czarnota, M. Pajek, D. Banaś, J.-Cl. Dousse, M. Berset, O. Mauron, Y.-P. Maillard, P. A. Raboud, D. Chmielewska, J. Rzadkiewicz, Z. Sujkowski, J. Hoszowska, M. Polasik, and K. Słabkowska, Radiat. Phys. Chem. **68**, 121 (2003).
[39] J. Rzadkiewicz, D. Chmielewska, Z. Sujkowski, J.-Cl. Dousse, D. Castella, D. Corminboeuf, J. Hoszowska, P. A. Raboud, M. Polasik, K. Słabkowska, and M. Pajek, Phys. Rev. A **68**, 032713 (2003).
[40] O. Keski-Rahkonen and M. O. Krause, Phys. Rev. A **15**, 959 (1977).
[41] J. Starosta, M. Polasik, and K. Słabkowska, Phys. Scripta **T156**, 014021 (2013).
[42] M. Czarnota, D. Banaś, M. Berset, D. Chmielewska, J.-Cl. Dousse, J. Hoszowska, Y.-P. Maillard, O. Mauron, M. Pajek, M. Polasik, P. A. Raboud, J. Rzadkiewicz, K. Słabkowska, and Z. Sujkowski, Eur. Phys. J. D **57**, 321 (2010).
[43] M. Czarnota, D. Banaś, M. Berset, D. Chmielewska, J.-Cl. Dousse, J. Hoszowska, Y.-P. Maillard, O. Mauron, M. Pajek, M. Polasik, P. A. Raboud, J. Rzadkiewicz, K. Słabkowska, and Z. Sujkowski, Phys. Rev. A **81**, 064702 (2010).
[44] M. Czarnota, D. Banaś, M. Berset, D. Chmielewska, J.-Cl. Dousse, J. Hoszowska, Y.-P. Maillard, O. Mauron, M. Pajek, M. Polasik, P. A. Raboud, J. Rzadkiewicz, K. Słabkowska, and Z. Sujkowski, Phys. Rev. A **88**, 052505 (2013).
[45] K. Słabkowska, J. Starosta, M. Polasik, M. Czarnota, M. Pajek, J.-Cl. Dousse, and J. Hoszowska, *Book of Abstracts, 43rd Conference of the European Group for Atomic Systems* (European Physical Society, Fribourg, Switzerland, 2011).
[46] M. Polasik, K. Słabkowska, J. Rzadkiewicz, K. Kozioł, J. Starosta, E. Wiatrowska-Kozioł, J.-Cl. Dousse, and J. Hoszowska, Phys. Rev. Lett. **107**, 073001 (2011).
[47] C. Merlet, X. Llovet, O. Dugne, S. Bremier, W. V. Renterghem, and R. Restani, Microchim. Acta **161**, 427 (2008).
[48] P. Indelicato, S. Boucard, and E. Lindroth, Eur. Phys. J. D **3**, 29 (1998).
[49] T. Mooney, E. Lindroth, P. Indelicato, E. G. Kessler, and R. D. Deslattes, Phys. Rev. A **45**, 1531 (1992).
[50] P. Indelicato and E. Lindroth, Phys. Rev. A **46**, 2426 (1992).
[51] R. D. Deslattes, E. G. Kessler, P. Indelicato, L. de Billy, E. Lindroth, and J. Anton, Rev. Mod. Phys. **75**, 35 (2003).
[52] J. L. Campbell and T. Papp, At. Data Nucl. Data Tables **77**, 1 (2001).
[53] M. Pajek, D. Banaś, D. Castella, D. Corminboeuf, J.-Cl. Dousse, Y.-P. Maillard, O. Mauron, P. A. Raboud, D. Chmielewska, I. Fijał, M. Jaskóła, A. Korman, T. Ludziejewski, J. Rzadkiewicz, Z. Sujkowski, J. Hoszowska, M. Polasik, and T. Mukoyama, Phys. Scr. **T92**, 382 (2001).
[54] B. Perny, J.-Cl. Dousse, M. Gasser, J. Kern, R. Lanners, Ch. Rheme, and W. Schwitz, Nucl. Instr. Meth. A **267**, 120 (1988).
[55] K. G. Dyall, I. P. Grant, C. T. Johnson, F. A. Parpia, and E. P. Plummer, Comput. Phys. Commun. **55**, 425 (1989).
[56] C. Froese Fischer, Atoms **2**, 1 (2014).
[57] J. A. Bearden, Rev. Mod. Phys. **39**, 78 (1967).